energies

Article

Design and Analysis of a Step-Up Multi-Port Converter Applicable for Energy Conversion in Photovoltaic Battery Systems

Siyuan Shi [1,2,†], Song Xu [1,2,†], Wei Jiang [3,†] and Seiji Hashimoto [2,*,†]

1 School of Automation, Jiangsu University of Science and Technology, Zhenjiang 212100, China; 221210301220@stu.just.edu.cn (S.S.); songxu@just.edu.cn (S.X.)
2 Department of Electronics and Informatics, Gunma University, Kiryu 376-8515, Japan
3 College of Intelligent Manufacturing, Yangzhou Polytechnic Institute, Yangzhou 215126, China; jiangw@ypi.edu.cn
* Correspondence: hashimotos@gunma-u.ac.jp
† These authors contributed equally to this work.

Abstract: Aiming at the problems of large power fluctuations and poor stability in photovoltaic and other new energy power generation systems, a step-up multiport converter (MPC) that can simultaneously connect low-voltage photovoltaic cells, batteries, and loads (independent loads or power grids) is proposed in this manuscript. According to the possible operating conditions of the system, the working principles are described in detail. Theoretical analysis based on different working modes is presented and a hybrid modulation control method including pulse width modulation (PWM) and phase shift modulation (PSM) are applied to realize energy transmission between photovoltaics, batteries, and power grids. A simulation model is built in the PSIM environment to validate each working state of the system and mode switching function. Experiments are carried out on an experimental platform using the dsPIC33FJ64GS606 digital microcontroller as the control center, and the experimental results successfully verify the system function and PWM + PSM control efficiency.

Keywords: step-up multiport converter; hybrid modulation control; PSIM

check for updates

Citation: Shi, S.; Xu, S.; Jiang, W.; Hashimoto, S. Design and Analysis of a Step-Up Multi-Port Converter Applicable for Energy Conversion in Photovoltaic Battery Systems. *Energies* **2024**, *17*, 223. https://doi.org/10.3390/en17010223

Academic Editor: Alon Kuperman

Received: 13 November 2023
Revised: 8 December 2023
Accepted: 28 December 2023
Published: 31 December 2023

1. Introduction

Recently, the contradiction between the increasing demand for energy and the depletion of fossil fuels has become increasingly serious, and the development and utilization of new energy resources is imminent [1,2]. An MPC as a new type of power electronic conversion device, effectively combines new energy and energy storage elements and improves the power density, reliability, and transient response speed of the converter. Many scholars and research institutions at home and abroad have performed much research on and improvement of the circuit topology of multiport converters and proposed some multiport converter circuit topologies. Ref. [3] proposed a multi-input converter based on forward and fly back converters. This converter is a time-sharing transmission type, but due to the circuit topology, the input current is discontinuous, and it is difficult to apply it in a high-power circuit. A non-isolated three-port DC-DC converter was pro-posed in [4], which can reduce the number of components and has a compact structure. Ref. [5] studied a topology structure in which two bidirectional DC-DC converters are connected to the DC bus. This structure can prolong the service life of the battery and improve the maximum power output capability of a hybrid energy storage system etc.

A multi-port converter of a new energy hybrid power supply system is proposed in the study. As a new branch of power electronic converter, compared with a traditional two-port converter, it can centrally control different energy forms and energy storage devices through a power unit to achieve energy transfer between different ports. It has the advantages of simple structure, low cost, and high reliability. With the continuous development and utilization of new energy, multi-port converters have been applied in a variety of power supply systems, such as new energy power supply systems represented by photovoltaic cells, fuel cells, etc. New energy grid-connected systems are widely used in hybrid power systems (such as electric vehicle electrical systems), uninterruptible power supply systems (UPS), commercial buildings, and residential buildings. The application of multi-port power conversion technology in new energy storage and power generation systems undoubtedly plays a huge role in the effective utilization of new energy and has great significance.

With the increasing depletion of traditional energy sources and the enhancement of people's awareness of environmental protection, renewable energy power generation is increasingly used [4,6–9]. Due to the intermittent and random characteristics of renewable energy such as photovoltaics, numerous grid connections will affect the safety and stability of the power grid and power quality [10–13] . Energy storage as a dispatchable resource applied to the power system can solve this problem well. The energy storage carriers of existing energy storage devices mainly use two types: batteries and super capacitors [12–16]. The energy density of the battery is high, but the power density is small, and it is not suitable for high-power and frequent charging and discharging [17,18]. Super capacitors, on the other hand, have fast response, high power output capability, and a long cycle life, but low energy density. The mixed use of batteries and super capacitors has great technical and economic advantages [19,20] and is an effective means to smooth the power fluctuation of the system.

This manuscript proposes a Step-Up multiport power generation system topology that can connect low-voltage photovoltaic cells, batteries, and loads at the same time. Considering the possible operating modes under different connection conditions, the proposed topology offers three working modes to realize step-up and bidirectional power transfer flow between three energy ports. On this basis, a hybrid modulation control scheme of duty ratio modulation and phase shift modulation (PWM + PSM) is proposed to control the system working mode for providing the possibility for power distribution of each port. The main contributions of this proposal are as follows: (1) Combine multiple energy sources to form a multi-energy hybrid power supply system; (2) Achieve stable, continuous, and efficient power supply; (3) Ensure the safe operation of the system and superior power transfer, while optimizing the power flow control at the control level.

The simulation model was built up in the PSIM environment and simulations of different working modes were carried out. Also, the experiments were carried out based on the experimental setup with the dsPIC33FJ64GS606 digital controller as the control center.

2. Configuration of the Step-Up Multiport Converter

2.1. Step-Up MPC Power Generation System Structure

The system structure of the proposed step-up multiport converter is shown in Figure 1 and is composed of three parts: isolated power unit, electric sensor and signal processing part, and digital control center. The proposed system can simultaneously connect low-voltage photovoltaic cells, storage batteries, and loads (this time using the isolated inverter to simulate the grid system) to realize energy exchange between the three energy ports.

Considering the maximum power tracking of the photovoltaic cell and system power balance, the designed power conversion system needs to meet the following requirements: (1) Dual power inputs including low-voltage level battery and photovoltaic panel. (2) Low-voltage level DC side needs to be isolated from high-voltage level side. (3) Bidirectional power flow control for power generation and energy storage.

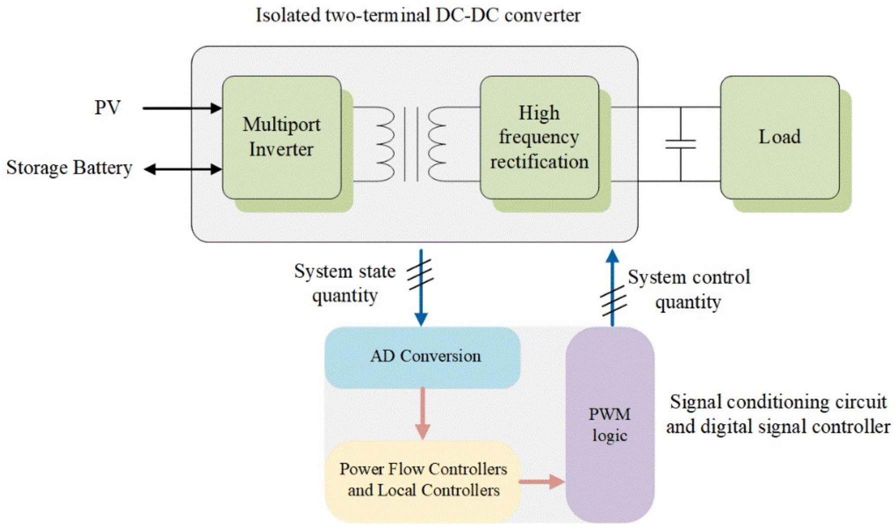

Figure 1. Multi-input low-voltage photovoltaic power generation system block diagram.

2.2. Three-Port Bidirectional DC-DC Converter Topology

As shown in Figure 2, the system can be divided into two parts: low voltage side (LVS) and high voltage side (HVS) which are isolated by the transformer T_r. The LVS is combined by a dual input full bridge inverter (HB1 and HB2) with two input ports P1 (connected to the battery) and P2 (connected to photovoltaic). Also, one bridge arm of the full bridge inverter (HB1) can also be used for combining a step-up and step-down converter with the input inductance L_s. The HVS has one output port P3 which provides the high voltage level DC output (P3) through half a bridge full controlled rectifier (HB3). The bridge arm HB1 can operate both in buck mode and boost mode, while HB1, HB2, and HB3 can realize bidirectional power transfer flow between the output port and the battery under different condition of P3.

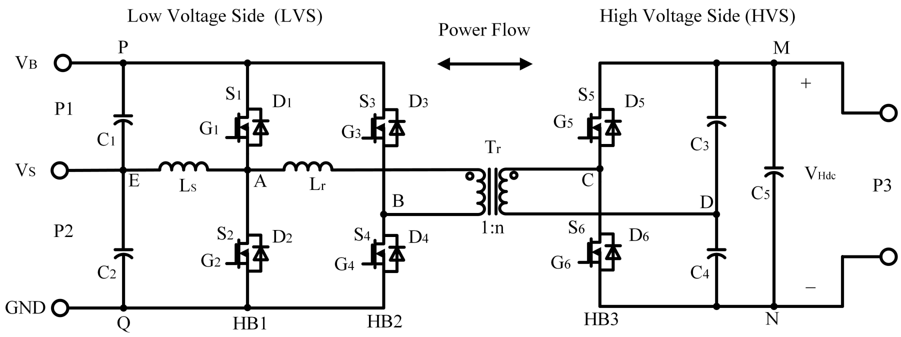

Figure 2. Step-Up Multiport Converter Main Circuit Topology.

3. System Working State Analysis

The dual-input buck-boost converter unit is shown in Figure 3. The topology consists of two input sources (the battery V_B and the photovoltaic cell V_S) and an output (the two ends of the bridge arm HB1), which are merged into the low-voltage side DC bus. By controlling the alternate conduction and shutdown of MOS transistor S_1 and MOS transistor S_2, the battery is charged and discharged. In addition, it provides energy for the low-voltage bus bar.

The output voltage V_{Ldc} can be calculated as:

$$V_{Ldc} = V_B + V_S = \frac{1}{1 - D_P} \cdot V_B = \frac{1}{D_P} \cdot V_S, \tag{1}$$

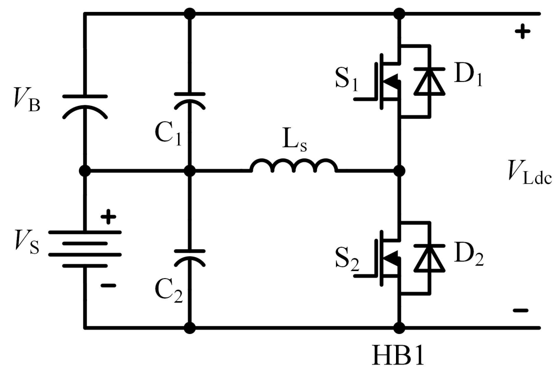

Figure 3. Dual Input Buck-Boost Converter Cell Topology.

To realize the topology proposed in this article, an asymmetric mixed modulation method is required. The AC voltage square wave signal from the secondary side is converted to the primary side of the transformer to obtain the equivalent circuit shown in Figure 4, where L_r is the leakage inductance of the transformer. The AC voltage signals of the primary and secondary sides of the high frequency transformer are V_P and V_S, respectively. By controlling the phase relationship between the two AC voltage signals, the magnitude and direction of the transmitted energy can be controlled. When the phase of V_P is ahead of V_S, the converter is in the power forward transmission mode at this time. Conversely, the converter is in reverse power transfer mode at this time.

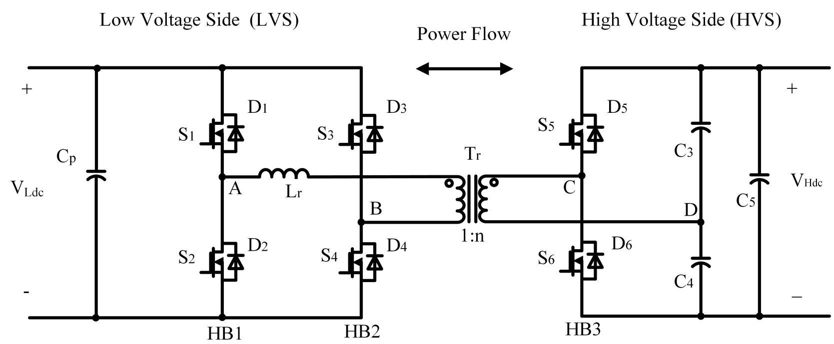

Figure 4. Bidirectional DC-DC Converter Equivalent Circuit.

In this proposal, an asymmetric hybrid modulation method is used to make the driving signals of S_1 and S_2 complementary. The duty cycle D_P of S_1 is calculated by the maximum power tracking algorithm, so that the driving signals of S_3 and S_4 are complementary, and the duty cycle of S_3 is the same as that of S_1. The phase shift angle between S_1 and S_3 is maintained at 180° , so that the driving signals of S_5 and S_6 are complementary, and the duty cycle is 0.5, that is, D_S = 0.5. Through the hybrid modulation method of duty cycle modulation and phase shift angle modulation (PWM + PSM), a certain phase shift angle is maintained between the driving signals of S_1 and S_5.

Figure 5 shows the ideal working waveform when the converter is in the power forward transmission mode, and the duty cycle of the primary full bridge is greater than 0.5, where v_{S1}, v_{S2}, v_{S3}, v_{S4}, v_{S5}, and v_{S6} are the voltage waveforms between the gates of S_1, S_2, S_3, S_4, S_5, and S_6, respectively. There is a 180° phase shift between the rising edge of v_{S1} and the rising edge of v_{S5}. The v_{AB} and v_{CD} are the midpoint voltage of the bridge arm of the primary side inverter and the midpoint voltage of the bridge arm of the secondary side half-bridge fully-controlled rectifier. i_r is the current flowing through the transformer, D_p is the duty cycle of S_1 and S_3, and D_s is the duty cycle of S_5, where D_s = 0.5. δ is the center phase shift angle between the high-level midpoint of V_{S1} and the high-level midpoint of v_{S5}. φ is the shift between the rising edge of v_{S5} and the rising edge of v_{S1} phase angle.

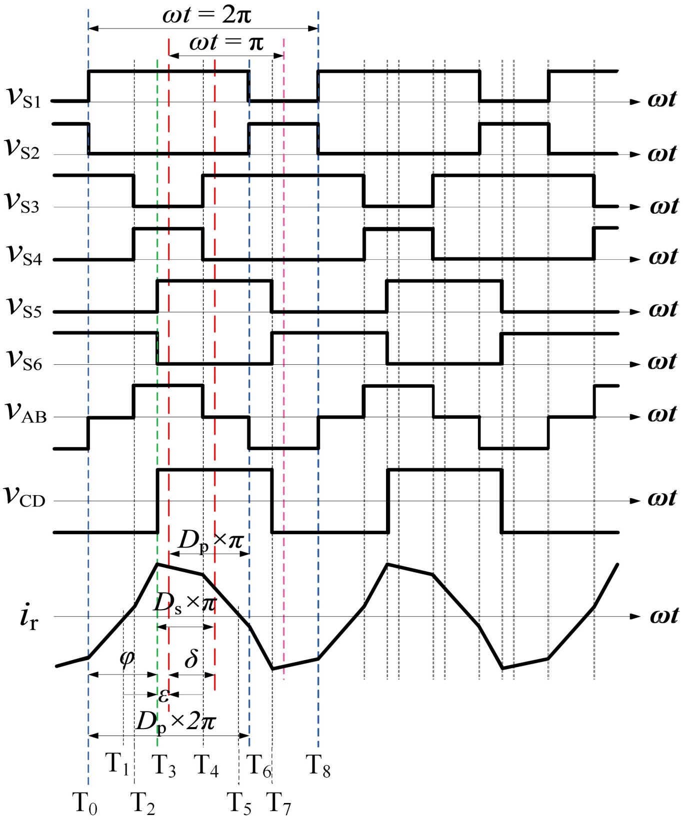

Figure 5. Waveform when the duty cycle D_P of the primary side is greater than 0.5.

According to the different working states of the switching tubes, each switching cycle is divided into eight stages, and the circuit states of each stage are shown in Figure 6a–h. The direction of the transformer current i_r takes the direction marked in Figure 4 as the positive direction, and the voltage across the inductor is recorded as V_r, and satisfies $V_r = V_p - V_s$. The voltages of capacitors C_3 and C_4 are recorded as V_{C3} and V_{C4} respectively, and the specified direction is positive and negative. After being converted to the original side, they are recorded as V_3 and V_4 respectively, satisfying $V_3 = V_{C3}/n$, $V_4 = V_{C4}/n$, where n is the voltage of the transformer turns ratio. Then there is:

$$V_f = L_f \frac{di_f}{dt} \xrightarrow{\theta = wt} V_f = wL_f \frac{di_f}{d\theta} \Rightarrow di_f = \frac{V_f}{wL_f} d\theta, \tag{2}$$

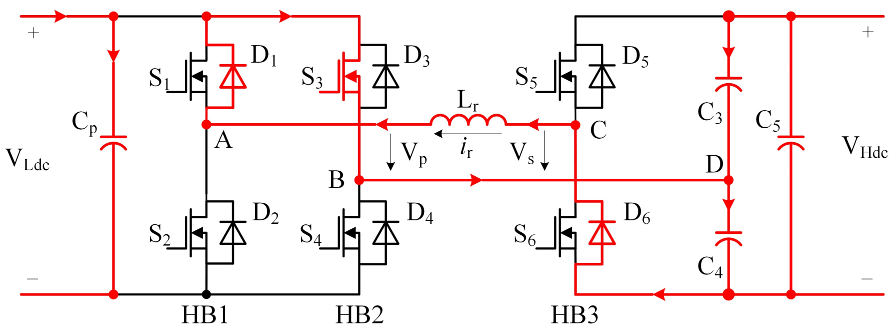

(**a**)

Figure 6. *Cont.*

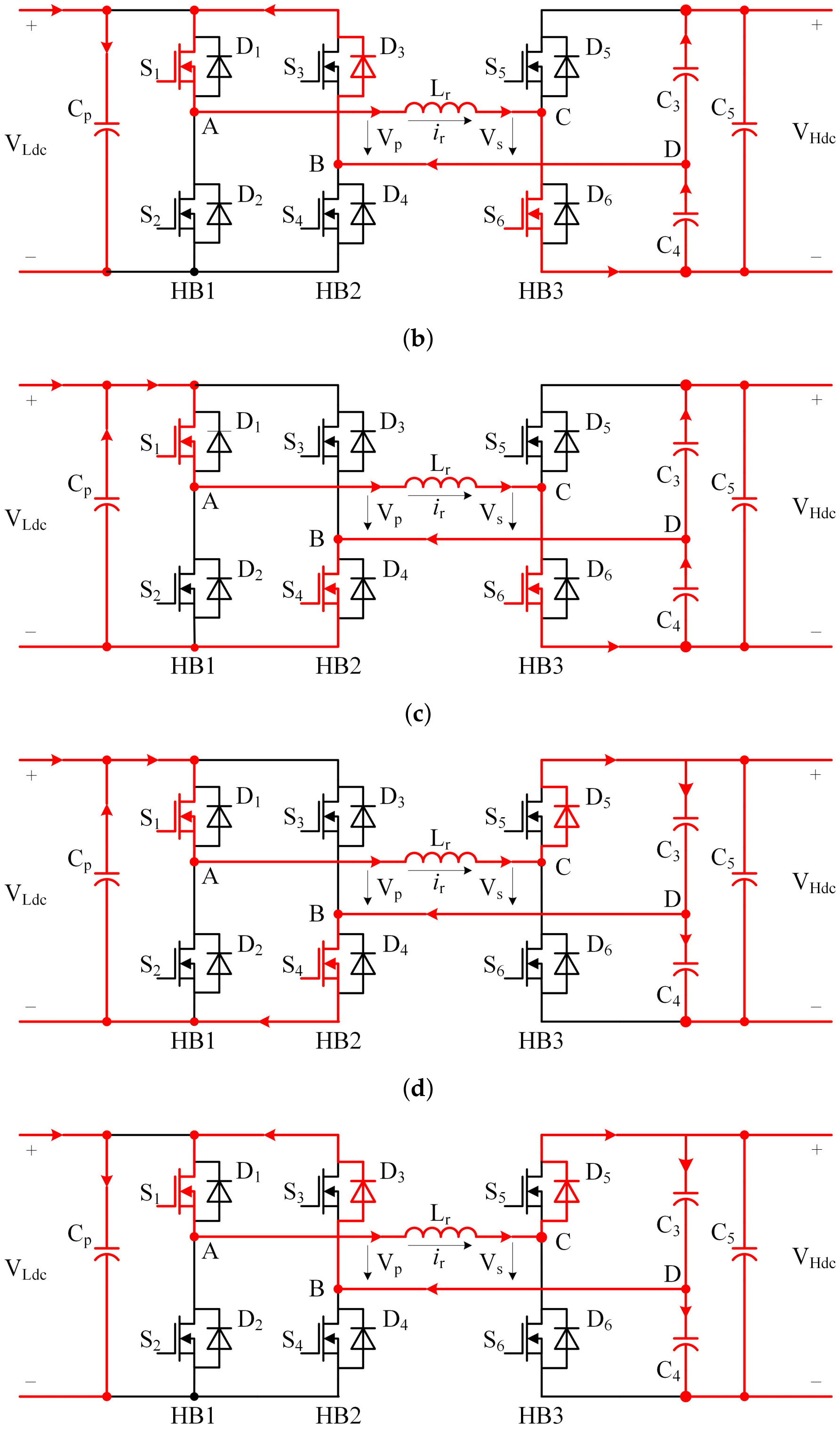

(**b**)

(**c**)

(**d**)

(**e**)

Figure 6. *Cont.*

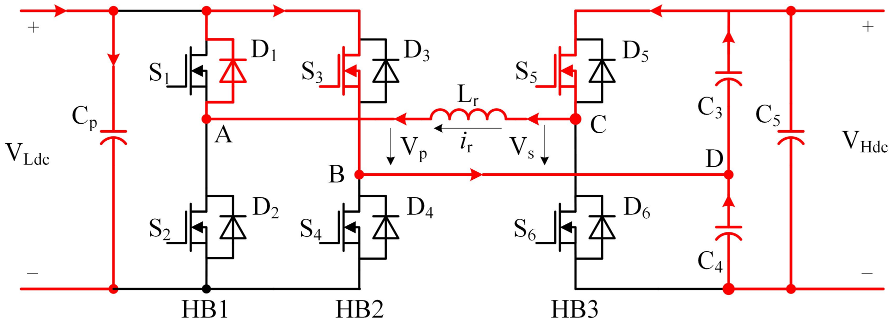

(**f**)

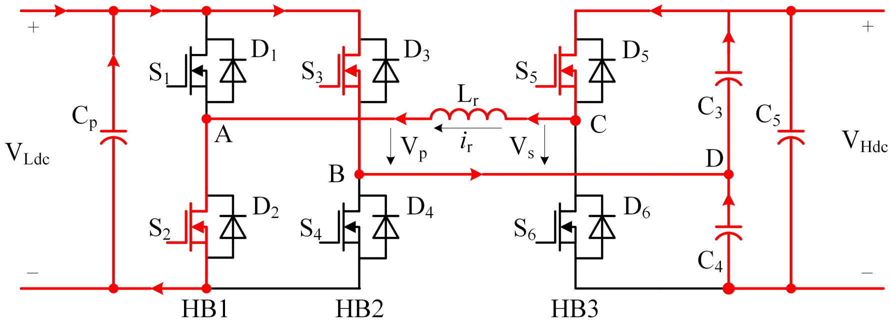

(**g**)

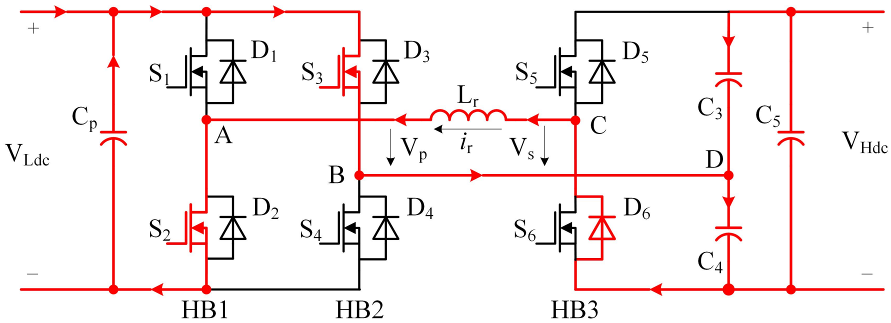

(**h**)

Figure 6. Power forward transfer working mode, the equivalent circuit in each state in one switching cycle when $D_p > 0.5$. (**a**) Equivalent circuit of bidirectional DC-DC converter in State 1. (**b**) Equivalent circuit of bidirectional DC-DC converter in State 2. (**c**) Equivalent circuit of bidirectional DC-DC converter in State 3. (**d**) Equivalent circuit of bidirectional DC-DC converter in State 4. (**e**) Equivalent circuit of bidirectional DC-DC converter in State 5. (**f**) Equivalent circuit of bidirectional DC-DC converter in State 6. (**g**) Equivalent circuit of bidirectional DC-DC converter in State 7. (**h**) Equivalent circuit of bidirectional DC-DC converter in State 8.

State 1 ($T_0 \sim T_1$): Trigger a conduction signal to S_1, S_3, and S_6. Since the inductor current is negative, S_1 and S_6 are both in the off state, S_3 is on, and the current flows from D_1, S_3, C_4, D_6, and L_r. However, at this time $V_p = 0$, $V_s = -V_4$, $V_r = V_p - V_s = V_4 > 0$, the inductor current increases linearly from a negative value, and the inductor current increases to zero at time T_1.

State 2 ($T_1 \sim T_2$): The trigger signals of all switch tubes remain unchanged, and the trigger signals of switch tubes S_1, S_3 and S_6 are still high-level conduction signals. At this time, the inductor current increases to a positive value, and the current changes from D_1, S_3, The flow through C_4, D_6, and L_r is changed to flow through S_1, L_r, S_6, C_4, and D_3. At this time, $V_p = 0$, $V_s = -V_4$, $V_r = V_p - V_s = V_4 > 0$, and the inductor current increases linearly. At the time of T_2, W_t = $(2D_p - 1)\pi$, the total amount of inductive current increase in the interval from T_0 to T_2 is:

$$\triangle i_r = \frac{V_4}{wL_r}(2D_p - 1)\pi, \tag{3}$$

State 3 ($T_2 \sim T_3$): Continue to turn on the signal to S_1 and S_6, turn off the signal to S_3, and turn on the signal to S_4. At this time, the current flows through S_1, L_r, S_6, C_4, and S_4, V_p = V_{Ldc}, V_s = $-V_4$, V_r = $V_p - V_s$ = V_{Ldc} + V_4 > 0, the inductor current continues to increase linearly. At the time of T_3, W_t = φ, the total amount of inductive current increase in the interval from T_2 to T_3 is:

$$\triangle i_r = \frac{V_{Ldc} + V_4}{wL_r}\left[\varphi - (2D_p - 1)\pi\right], \tag{4}$$

State 4 ($T_3 \sim T_4$): Continue to turn on the signal to the switch tubes S_1 and S_4, turn off the signal to S_5, and turn on the signal to S_6. Since the inductor current is positive, the current flows through S_1, L_r, D_5, C_3, and S_4, at this time, V_p = V_{Ldc}, V_s = V_3, V_r = $V_p - V_s$ = $V_{Ldc} - V_3$. At the time of T_3, W_t = π, the total amount of increase in the inductor current in the interval from T_3 to T_4 is:

$$\triangle i_r = \frac{V_{Ldc} - V_3}{wL_r}(\pi - \varphi), \tag{5}$$

State 5 ($T_4 \sim T_5$): Continue to turn on the signal to the switch tubes S_1 and S_5, turn off the signal to S_4, and turn on the signal to S_3. Since the inductor current is positive, the current flows through S_1, L_r, D_5, C_3, and D_3, at this time, V_p = 0, V_s = V_3, V_r = $V_p - V_s$ = $-V_3$ < 0, the inductor current decreases linearly, and the inductor current decreases to zero at time T_5.

State 6 ($T_5 \sim T_6$): The trigger signals of all switch tubes remain unchanged, and the trigger signals of switch tubes S_1, S_3, and S_5 are still high-level conduction signals. At this time, the inductor current decreases to a negative value, and the current changes from S_1, L_r, D_5, C_3, and D_3 flow through D_1, S_3, C_3, S_5, and L_r. At this time, V_p = 0, V_s = V_3, V_r = $V_p - V_s$ = $-V_3$ < 0, and the inductor current continues to decrease linearly. At the moment of T_6, W_t = $2D_p\pi$, the total increase of the inductor current in the interval of $T_4 \sim T_6$ is:

$$\triangle i_r = \frac{-V_3}{wL_r}(2D_p - 1)\pi, \tag{6}$$

State 7 ($T_6 \sim T_7$): Continue to turn on the signal to the switch tubes S_3 and S_5, turn off the signal to S_1, and turn on the signal to S_2. At this time, the current flows through S_3, C_3, S_5, L_r, and S_2, V_p = $-V_{Ldc}$, V_s = V_3, V_r = $V_p - V_s$ = $-V_{Ldc} - V_3$ < 0, the inductor current continues to decrease linearly, at the time of T_7, W_t = $\pi + \varphi$, the total increase of the inductor current in the interval from T_6 to T_7 is:

$$\triangle i_r = \frac{-V_{Ldc} - V_3}{wL_r}(\pi + \varphi - 2D_p\pi), \tag{7}$$

State 8 ($T_7 \sim T_8$): Continue to turn on the signal to the switch tubes S_2 and S_3, turn off the signal to S_5, and turn on the signal to S_6. At this time, the current flows through S_3, C_4, D_6, L_r, and S_2, V_p = $-V_{Ldc}$, V_s = $-V_4$, V_r = $V_p - V_s$ = $-V_{Ldc}$ + V_4 > 0, the inductor current increases linearly, at the moment of T_8, W_t = 2π, the total increase of the inductor current in the interval between T_7 and T_8 is:

$$\triangle i_r = \frac{-V_{Ldc} + V_4}{wL_r}(\pi - \varphi), \tag{8}$$

According to $i_r(0) = -i_r(\pi)$, $i_r(2D_p\pi - \pi) = -i_r(2D\pi)$, $i_r(\varphi) = -i_r(\pi + \varphi)$, the expression of its initial state can be deduced:

$$\begin{cases} i_r(0) = -i_r(\pi) = \frac{-V_{Ldc}}{2wL_r}(2\pi - 2D_p\pi) + \frac{V_3}{2wL_r}(\pi - \varphi) - \frac{V_4}{2wL_r}\varphi \\ i_r(2D_p\pi - \pi) = -i_r(2D_p\pi) = \frac{V_{Ldc}}{2wL_r}(2\pi - 2D_p\pi) - \frac{V_3}{2wL_r}(\pi - \varphi) + \frac{V_4}{2wL_r}(2\pi + \varphi - 4D_p\pi), \\ i_r(\varphi) = -i_r(\pi + \varphi) = \frac{V_{Ldc}}{2wL_r}(2D_p\pi - 2\varphi) - \frac{V_3}{2wL_r}(\pi - \varphi) - \frac{V_4}{2wL_r}\varphi \end{cases} \quad (9)$$

The working waveform of the circuit when the duty ratio D_p of the primary side is less than 0.5 is shown in Figure 7. In reverse flow mode, the analysis process is similar to when D_p is greater than 0.5.

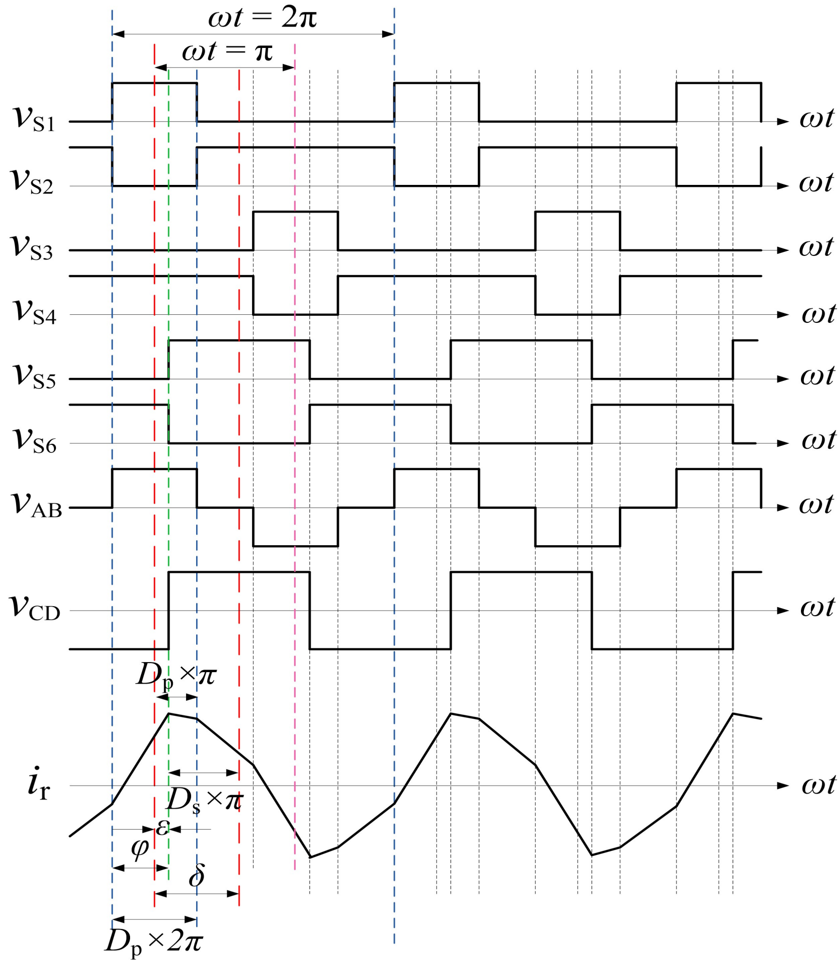

Figure 7. Waveform when the duty cycle D_p of the primary side is less than 0.5.

From the waveform analysis in Figures 5 and 7, it can be seen that when the duty cycle $D_p > 0.5$ and $D_p < 0.5$, the relationship between D_p, D_s, δ, φ, and ε is:

$$\begin{cases} \varphi + \varepsilon = \frac{D_p}{2} \times 2\pi \\ \delta + \varepsilon = \frac{D_s}{2} \times 2\pi \end{cases} \quad D_p > 0.5, \quad (10)$$

$$\begin{cases} \varphi - \varepsilon = \frac{D_p}{2} \times 2\pi \\ \delta - \varepsilon = \frac{D_s}{2} \times 2\pi \end{cases} \quad D_p < 0.5, \quad (11)$$

From the above relationship, it can be concluded that regardless of whether $D_p > 0.5$ or $D_p < 0.5$, the following is satisfied:

$$\varphi = \delta + (\frac{D_p}{2} - \frac{D_s}{2}) \times 2\pi, \quad (12)$$

The following formula can be obtained:

$$D_\varphi = D_\delta + (\frac{D_p}{2} - \frac{D_s}{2}), \tag{13}$$

Through the above relationship, the phase shift angle φ between the rising edge of v_{S5} and the rising edge of vs1 can be calculated according to the current primary side duty cycle D_p, secondary side duty cycle D_s, and the central phase shift angle δ between the high−level midpoint of vs1 and the high-level midpoint of v_{S5}.

The working mode of the proposed system is decided by the energy connection condition of ports P1, P2, and P3, mainly divided into three modes with each mode having a different power flow. Mode I: Both P1 and P2 transfer power to the load P3 through the converter. This mode appears when the power provided by the PV is less than the rated power of the load. In this mode, the battery is in discharging state. Mode II: The PV provides energy to the load (P3) and battery (P2) which means that the power provided by photovoltaics is greater than the rated power of the load, and the remaining energy is charged to the energy storage system. In this mode, the battery is in charging state. Mode III: This mode is the energy feedback mode from the load, thus, both PV and load transfer the energy to the storage battery. In this mode, the battery moves from the discharging state to the charging state.

4. Control Strategy

In order to realize the MPPT control of the PV port and the converted power with direction control, a pulse with modulation and a phase shift (PWM + PSM) control strategy is applied for controlling the proposed conversion system, as shown in Figure 8, where the PWM duty D_p is used for MPPT control and the phase shift δ is used for power control through PI controller C_v.

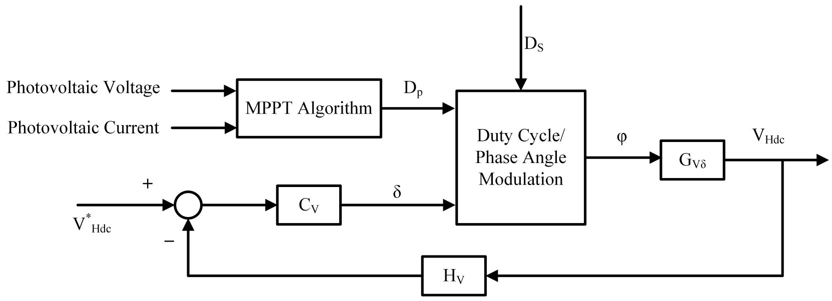

Figure 8. Block diagram of the PWM + PSM hybrid modulation scheme.

The system control process of hybrid modulation using duty cycle modulation and phase shift modulation can be divided into two parts. One is the duty cycle modulation process, that is, the photovoltaic MPPT algorithm. The other is the phase shift angle modulation process, that is, the output voltage control.

Photovoltaic maximum power point tracking (MPPT) implementation method: the duty cycle disturbance observation method is adopted on the primary side, and it is sent to the dsPIC33F microcontroller after sampling through the photovoltaic cell voltage and current sampling circuit. The dsPIC33F microcontroller will calculate the power according to the current sampled photovoltaic cell voltage and current, and obtain the current photovoltaic cell output power, compare it with the power at the previous moment, and make the current working point move to the maximum power point by disturbing the duty cycle of the primary full-bridge inverter. In this way, the photovoltaic maximum power tracking (MPPT) is realized, and the duty cycle D_p of the primary full−bridge inverter is obtained at the current maximum power.

Closed-loop control process of output voltage on the high side: the output voltage V_{Hdc} of the secondary side half-bridge full controlled rectifier is sampled, and the output voltage is sent to the voltage controller after comparing it with the target value of the output voltage. The output δ of the voltage controller is sent to the duty cycle/phase shift angle modulator, and the duty cycle/phase-shift angle modulator is combined with the duty cycle D_p of the current primary side full-bridge inverter and the duty cycle D_s of the secondary side half-bridge full controlled rectifier to calculate the phase-shift angle φ between the rising edge of the modulation signal v_{s5} of the half-bridge full controlled rectifier relative to the rising edge of the primary-side modulation signal v_{s1}. The amplitude of the output voltage and the magnitude and direction of the transmission power are controlled by adjusting the phase-shift angle.

Calculate the phase shift angle φ between the rising edges according to the primary duty cycle D_p, the secondary duty cycle D_s, and the central phase shift angle δ. Convert δ to the corresponding φ. The conversion formula is as in (14).

$$\varphi = \delta + (\frac{D_p}{2} - \frac{D_s}{2}) \times 2\pi, \tag{14}$$

By adjusting the duty ratio D_p of the dual-input inverter on the primary side, the maximum power tracking of the input photovoltaic and the function of the dual-input inverter are realized. Meanwhile, the phase shift angle is adjusted to realize output voltage stabilization and control of the transferred power as well as its flow direction.

System Simulation and Analysis

In order to verify the working mode and control strategy of the system, a closed-loop simulation of the step-up multiport converter (MPC) proposed in this paper is carried out in the PISM software (9.14 Professional) , and the simulation circuit diagram is shown in Figure 9.

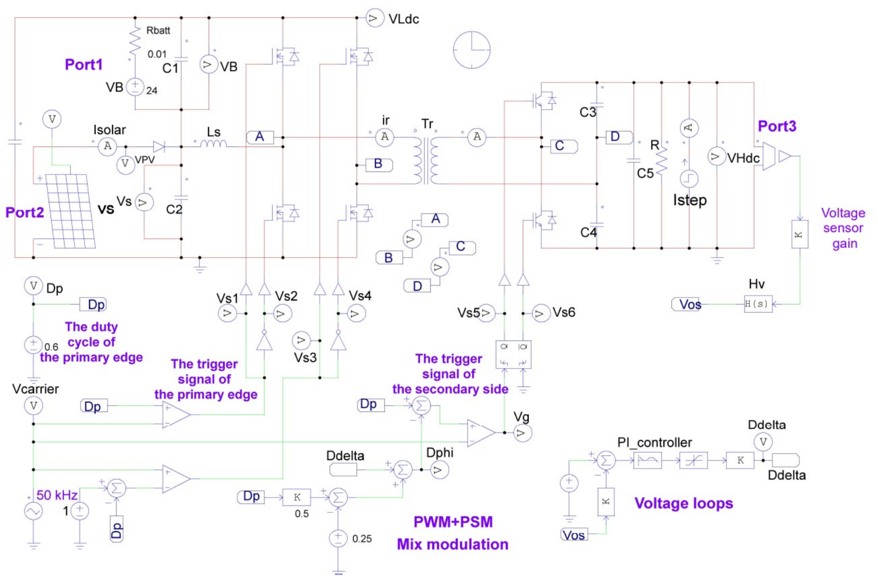

Figure 9. Schematic diagram of circuit simulation.

As shown in Figure 9, the circuit simulation schematic consists of two parts: The main circuit part and the control circuit part. The main circuit mainly includes two input sources, V_B and V_S, access port 1 and port 2 respectively, a full-bridge inverter, a transformer, a half-bridge rectifier, a voltage regulator capacitor, and load.

The control circuit mainly includes a reference carrier signal, a voltage sampling circuit, a voltage control circuit, a PWM + PSM hybrid modulation circuit, a primary-side trigger signal generation circuit, and a secondary-side trigger signal generation circuit. The H_v is the first-order low-pass filter transfer function; The PI controller in the voltage control loop is a PI algorithm controller with two poles and two zeros; D_{delta} and D_{phi} are D_δ and D_φ, respectively, which appear in the previous sections; D_p is the primary duty cycle.

The principle of trigger signal generation of the primary and secondary sides is simulated and verified in PSIM. The primary side duty cycle is given as D_p = 0.6 and

D_{phi} = 0.1 (φ = 0.2π) for simulation, and the waveform generated by the primary trigger signal is shown in Figure 10. The waveform generated by the secondary trigger signal is shown in Figure 11. The simulation results are consistent with the previous analysis and verify the feasibility.

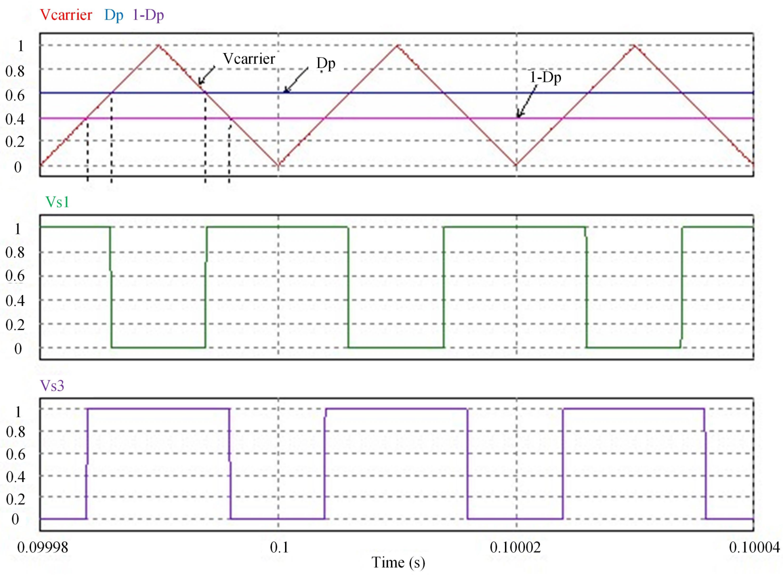

Figure 10. The primary side trigger signal generates a simulation diagram.

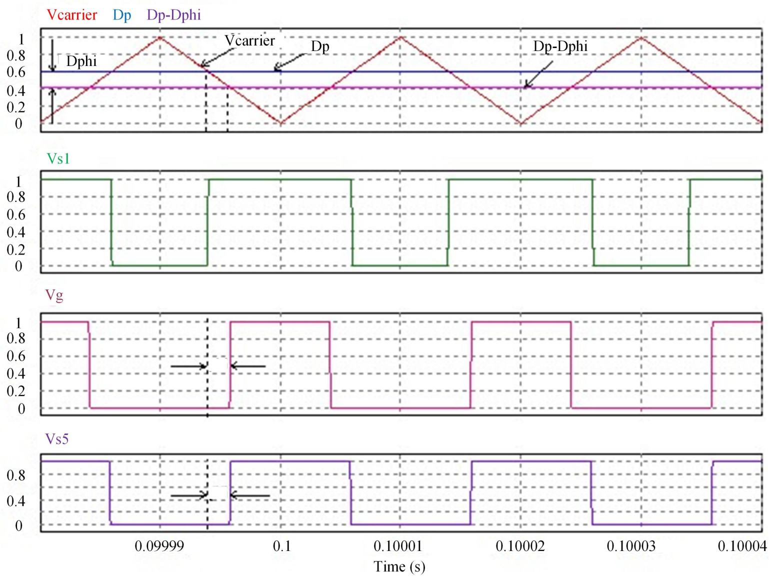

Figure 11. Timing diagram of the secondary drive signal.

Table 1 shows the circuit simulation parameter settings.

In this state, the step current source I_{step} is set to an invalid state, the output voltage of the control high-voltage side is 200 V, and the load is a resistive load. At this time, the photovoltaic cell works at the maximum power point, and the photovoltaic provides 200 W of power, and it can be seen that the output power of the photovoltaic cell is less than the power required by the load, and the combined power supply of the battery is required to meet the power demand of the load side.

Table 1. Simulation Parameter Settings.

Circuit Parameters	Value	Circuit Parameters	Value
Output rated power p	500 W	Battery voltage V_b	24 V
Photovoltaic cell maximum power voltage V_{Sm}	36 V	Photovoltaic cell maximum power current I_{Sm}	5.55 A
Output voltage V_{Hdc}	200 V	Output resistance R	80 Ω
First filter capacitor C_1	40 uF	Second filter capacitor C_2	100 uF
Input inductance L_s	25 uH	Stabilizer capacitor C_5	0.1 uF
Capacitance C_3	470 uF	Capacitance C_4	470 uF
Transformer leakage inductance L_r	15 uH	Transformer turns ratio n	1.67
On-off level f_S	50 KHz	Primary Duty Cycle D_p	0.6

Figure 12 shows the simulated waveform of the output voltage of the high voltage side. As can be seen from the simulation results, the final output voltage is stabilized at 200V and the output voltage on the high side is effectively controlled. The battery current is positive, which proves that the battery is in a discharged state.

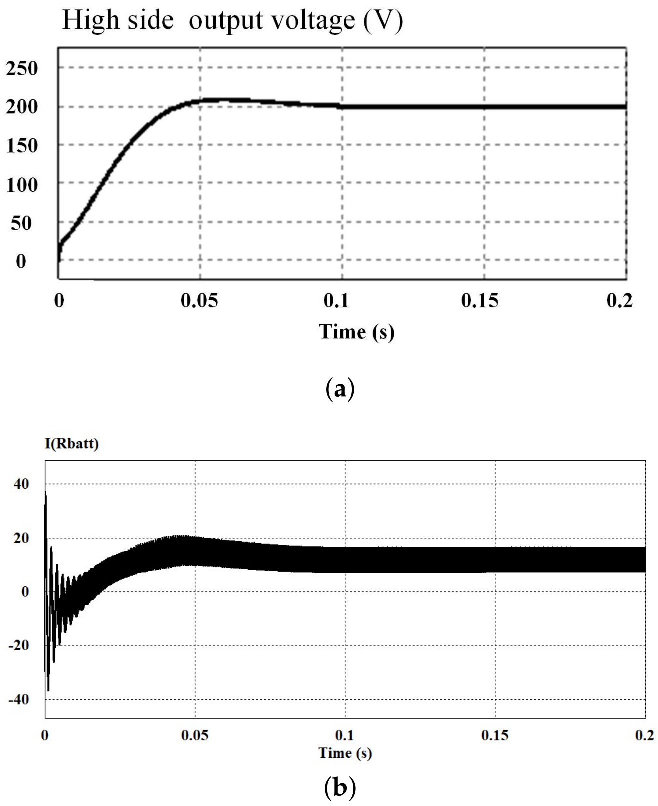

Figure 12. Simulation waveform. (**a**) Output voltage waveform. (**b**) Battery current waveform.

5. Expiremental Verification

Based on the theoretical analysis and simulation verification result, an experimental prototype was established using the dsPIC33FJ64GS606 the as digital controller. The device is mainly composed of a main circuit, a control circuit, and an auxiliary power circuit. The control circuit includes a chip and its peripheral circuits, a sampling circuit, and a driving circuit. The experimental platform is shown in Figure 13. Table 2 shows the circuit experimental parameters.

The PWM trigger signal generation of the primary and secondary side is experimentally verified, and the duty cycle of the primary side is given as 0.6, the duty cycle of the secondary side is 0.5, the dead time t_d = 0.5 us, the phase shift angle φ = 0.4π (the corresponding central phase shift angle δ = 0.3π), and the corresponding waveform is obtained, as shown in Figure 14.

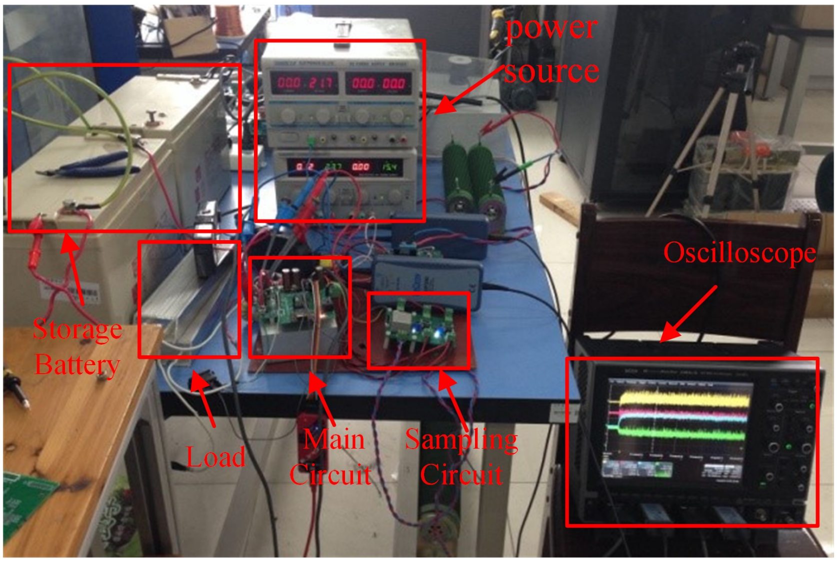

Figure 13. Step-up MPC power generation system hardware test environment.

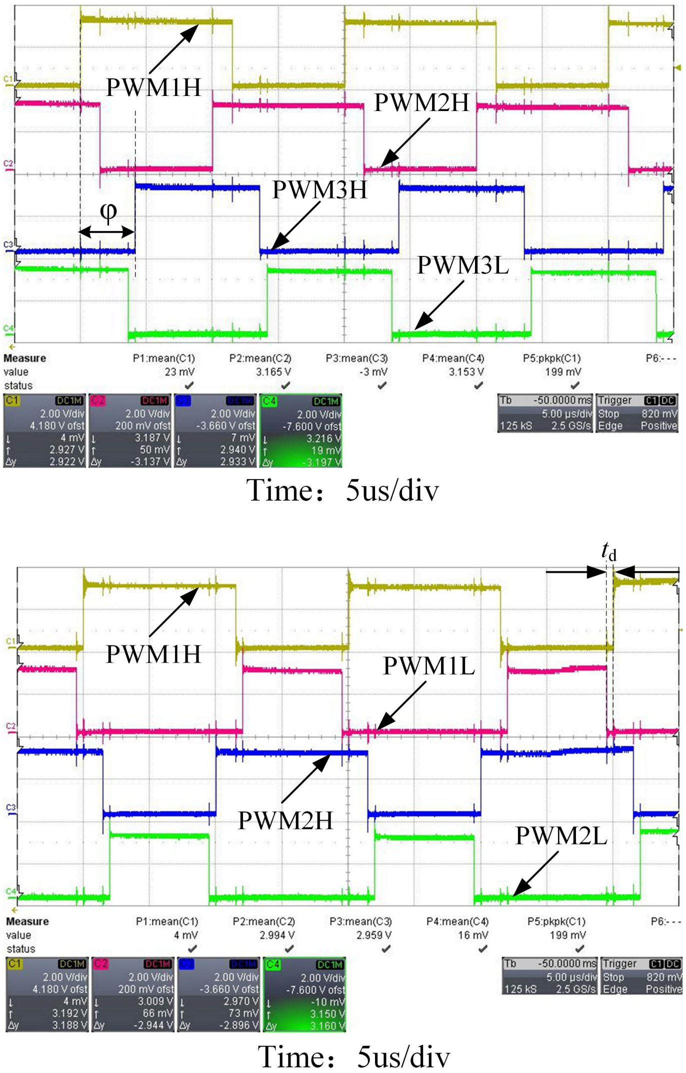

Figure 14. The PWM signal waveform output by the PWM modulel.

Table 2. Experimental Parameter Settings.

Circuit Parameters	Value	Circuit Parameters	Value
Output resistance R	160 Ω	Battery voltage V_b	12.5 V
Photovoltaic cell maximum power voltage V_{Sm}	22 V	Photovoltaic cell maximum power current I_{Sm}	3 A
Output voltage V_{Hdc}	100 V	Primary Duty Cycle D_p	0.6
Input inductance L_s	25 uH	Stabilizer capacitor C_5	0.1 uF
On−off level f_S	50 KHz	Capacitance C_4	470 uF

As shown in Figure 15 (all four channels are 2 V/div), the PWM signal waveform with a frequency of 50 kHz output by the PWM module pin of dsPIC, in which the phase shift angle between the rising edges of the two waveforms of PWM1H and PWM3H is φ, is consistent with the set value requirements, and the PWM and phase shift operations can be completed without consuming any DSP resources.

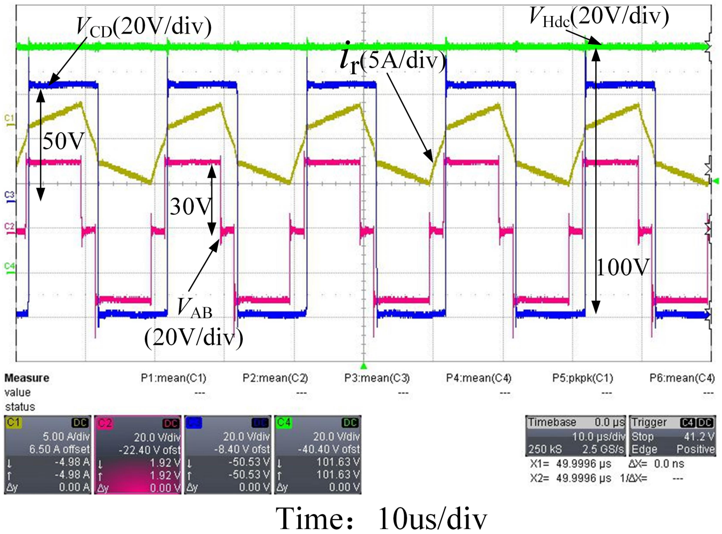

(**a**)

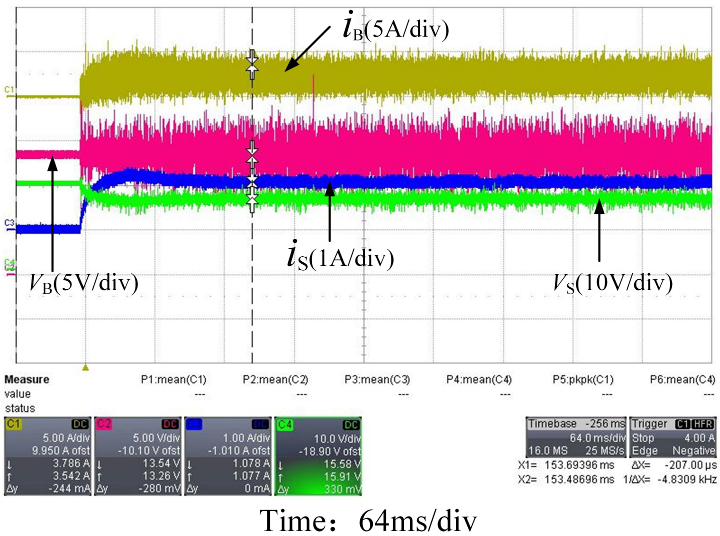

(**b**)

Figure 15. Experimental results, (**a**) Start-up waveform, (**b**) Battery voltage and current, power supply voltage and current.

Figure 16 shows the corresponding gate-to-source trigger signal waveform (10 V/div for all three channels) after the PWM signal output by the PWM module is passed through the drive circuit.The figure shows the waveforms of the gate trigger voltages v_{S1}, v_{S3} and v_{S5} obtained by PWM1H, PWM2H, and PWM3H after the corresponding drive circuits, and the phase shift angle between the rising edges of the waveforms of v_{S1} and v_{S5} is φ.

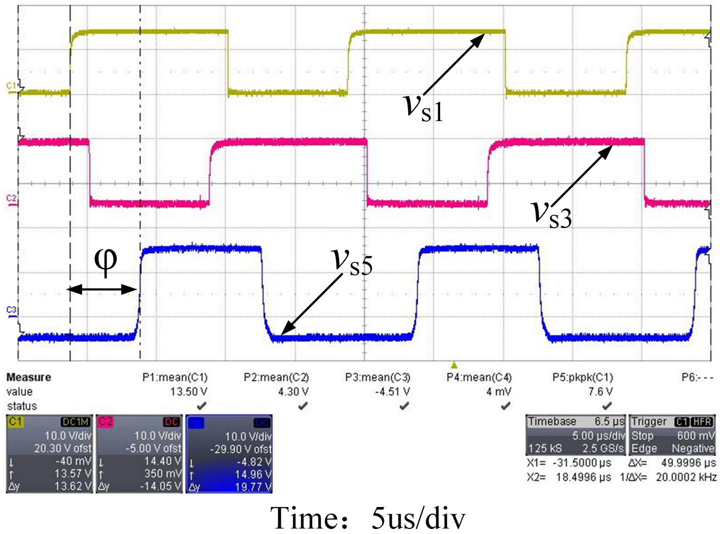

Figure 16. Primary secondary side switch gate source trigger signal waveform.

As can be seen from Figure 16, the voltage of v_{S1} and v_{S3} is 0–13.5 V, which meets the output requirements of the IR2110S and meets the opening and closing voltage requirements of the primary side MOS tube; the voltage of v_{S6} is -5–+15 V, which meets the output requirements of KD301L, and also meets the opening and closing voltage requirements of the secondary side MOS tube.

In the experiment, a series combination of a DC power supply and a resistor is used to simulate photovoltaic cell access P2. P1 is connected to a 12.5 V battery and P2 is connected to a 22 V voltage source to simulate the PV panel. The output port P3 is connected to the load which is represented by a 160 ohm resistor. The duty cycle D_p of the LVS is set to 0.6, and the controlled output voltage is set to 100 V. The experimental results of the steady-state are shown in Figure 15.

From the steady-state experimental results shown in Figure 15a, the HVS output voltage V_{Hdc} of 100 V has been successfully controlled. From the waveforms of voltage V_{AB} and voltage V_{CD} , it can be seen that the high-level center of V_{AB} is ahead of the high$-$level midpoint of V_{CD}, that is, the phase of the primary side is ahead of the secondary side, the primary side of the transformer transmits power to the secondary side, and the system is in the power forward transmission state.

The battery current shown in Figure 15b is positive at about 3 A, thus, the battery is working under discharging mode. The experimental results are in line with the theoretical analysis and simulation, and the control system effectiveness has been successfully verified.

6. Conclusions

In the research of Step-Up MPC, photovoltaic cells and batteries are used as input energy sources, and a Step-Up MPC power generation system topology that can simultaneously connect low-voltage photovoltaic cells, batteries, and loads (independent loads or grids) is proposed to realize energy exchange between photovoltaics, batteries, and the grid. The detailed process of this topology generation is given. According to the power flow between the ports, their working principles are explained in detail, and their working process is analyzed, calculated, and modeled in combination with the working waveform of the circuit. On this basis, a hybrid modulation control scheme of duty cycle modulation and phase shift modulation is proposed, and the working states and mode switching are simulated and verified in the PSIM simulation environment. Finally, a Step-Up MPC device is designed and manufactured, and the effectiveness of the PWM + PSM modulation and control scheme under dual-input power generation conditions is verified through experiments.

Compared with existing technology, the beneficial effect of the Step-Up MPC circuit topology proposed in this paper is that this it can be used as a buck-boost circuit by using S1 and S2 with the input inductance, and at the same time, S1, S2, S3, and S4 cooperate to act as a buck-boost circuit to the inverter function, thus saving a group of MOS tubes and saving costs. By adjusting the duty cycle of the primary side inverter, the maximum power tracking of photovoltaics can be realized, and the normal operation of the inverter circuit can be ensured. Furthermore, by sampling the output voltage of the secondary side, the phase shift angle of the primary-side inverter and the secondary side rectifier is adjusted to realize output voltage regulation and power flow control, which can be used in multi-input low-voltage photovoltaic power generation systems.

Author Contributions: Conceptualization, S.X. and W.J.; methodology, S.H.; software, S.S.; validation, S.X., W.J. and S.H.; formal analysis, S.S.; investigation, S.X.; resources, S.S.; data curation, S.S.; writing—original draft preparation, S.S.; writing—review and editing, S.X.; visualization, W.J.; supervision, S.H.; project administration, W.J.; funding acquisition, S.H. All authors have read and agreed to the published version of the manuscript.

Funding: This research received no external funding

Data Availability Statement: Data is contained within the article.

Conflicts of Interest: The authors declare no conflict of interest.

References

1. Wang, L.; Meng, F.; Sun, Z.; Yang, S.; Yang, W. An Adaptive Hysteresis Sliding Mode Control Method for Double-Switch Buck-Boost Converter. In Proceedings of the IEEE Transportation Electrification Conference and Expo, Asia-Pacific, Harbin, China, 7–10 August 2017.
2. Vahedi, H.; Sheikholeslami, A.; Bina, M.T. A Novel Hysteresis Bandwidth (NHB) Calculation to Fix the Switching Frequency Employed in Active Power Filter. In Proceedings of the IEEE Applied Power Electronics Colloquium, Johor Bahru, Malaysia, 18–19 April 2011; pp. 155–158.
3. Matsuo, H.; Lin, W.; Kurokawa, F.; Shigemizu, T.; Watanabe, N. Characteristics of the Multiple-Input Dc-Dc Converter. In Proceedings of the 24th Annual Power Electronics Specialists Conference, Washington, DC, USA, 20–24 June 2004; Volume 51, pp. 625–631.
4. Wu, H.; Sun, K.; Ding, S.; Xing, Y. Topology Derivation of Nonisolated Three-Port DC-DC Converters from DIC and DOC. *IEEE Trans. Ind. Electron.* **2013**, *28*, 3297–3307. [CrossRef]
5. Sun, Z.Y.; Bae, S. Multiple-Input Soft-Switching Step-Up/down Converter for Renewable Energy Systems. In Proceedings of the 7th International Conference on Renewable Energy Research and Applications, Paris, France, 14–17 October 2018.
6. Chen, X.; Shi, M.; Zhou, J.; Zuo, W.; Chen, Y.; Wen, J.; He, H. Consensus-based Distributedcontrol for Photovoltaic-Battery Units in A DC Microgrid. *IEEE Trans. Ind. Electron.* **2019**, *66*, 7778–7787. [CrossRef]
7. Tan, Z.K.; Cheng, L.F.; Shi, S.Y.; Wang, W.R.; Xu, W.F.; Hua, J.X.; Yu, T. Discussion on Key Technologies of Energy Internet Access Equipment. *Power Syst. Prot. Control* **2019**, *47*, 140–152.
8. Ye, Z.M.; Jian, P.; Sen, P. Control of series parallel resonant converter with two different input voltage sources. In Proceedings of the 37th Annual IEEE Power Electronics Specialists Conference, Jeju, Korea, 18–22 June 2006.
9. Alexis, K.; Philip,T.K. Multiple-input DC-DC converters to enhance local availability in grids using distributed generation resources. In Proceedings of the 22th Annual IEEE Applied Power Electronics Conference, Anaheim, CA, USA, 25 February 2007.
10. Qian, Z.J.; Abdel-Rahman, O.; Batarseh, I. An Integrated Four-Port DC/DC Converter for Renewable Energy Applications. *IEEE Trans. Ind. Electron.* **2010**, *25*, 1877–1887. [CrossRef]
11. Xu, C.; Gu, Y.J.; Luo, H.Z.; Hu, Y.H.; Zhao, Y.; Li, W.H.; He, X.N. Performance Analysis of Coupled Inductor based Multiple-Input DC-CD Converter with PWM Plus Phase-Shift (PPS) Control Strategy. In Proceedings of the ECCE Asia Downumder (ECCE Asia), Melbourne, Australia, 3–6 June 2013; pp. 994–998.
12. Chen, Y.; Li, P.; Li, Z. DC/DC half-bridge SST based on energy router. IOP *Conf. Ser. Earth Environ. Sci.* **2020**, *467*, 012100. [CrossRef]
13. Jiang, W.; Fahimi, B. Active Current Sharing and Source Management in Fuel Cell-Battery Hybrid Power System. *IEEE Trans. Ind. Electron.* **2010**, *57*, 752–761. [CrossRef]

14. Wai, R.; Lin, C.; Liu, L.; Chang, Y. High-efficiency single-stage bidirectional converter with multi-input power sources. *Electr. Power Appl.* **2007**, *1*, 763–777. [CrossRef]
15. Jiang, W.; Fahimi, B. Multi-port power electronic interface for renewable energy sources. In Proceedings of the 24th Annual IEEE Applied Power Electronics Conference and Exposition, Washington, DC, USA, 15–19 February 2009; pp. 347–352.
16. Rostami, S.; Abbasi, V.; Talebi, N.; Kerekes, T. Three-port DC-DC converter based on quadratic boost converter for stand-alone PV-battery systems. *IET Power Electron.* **2020**, *13*, 2106–2118. [CrossRef]
17. Shanmugam, S.K.; Ramachandran, S.; Arumugam, S.; Pandiyan, S.; Nayyar, A.; Hossain, E. Design and implementation of improved three port converter and B4-inverter fed brushless direct current motor drive system for industrial applications. *IEEE Access* **2020**, *8*, 149093–149112. [CrossRef]
18. Khan, S.R.; Pavuluri, S.K.; Cummins, G.; Desmulliez, M.P. Wireless power transfer techniques for implantable medical devices: A review. *Sensors* **2020**, *20*, 3487. [CrossRef] [PubMed]
19. Zhou, Z.; Zhang, L.; Liu, Z.; Chen, Q.; Long, R.; Su, H. Model predictive control for the receiving-side DC-DC converter of dynamic wireless power transfer. *IEEE Trans. Power Electron.* **2020**, *35*, 8985–8997. [CrossRef]
20. Feng, Z.; Clerckx, B.; Zhao, Y. Waveform and beamforming design for intelligent reflecting surface aided wireless power transfer: Single-user and multi-user solutions. *IEEE Trans. Wirel. Commun.* **2022**, *21*, 5346–5361. [CrossRef]